The shear mode of multilayer graphene

P. H. Tan[1]*, W. P. Han[1], W. J. Zhao[1], Z. H. Wu[1], K. Chang[1], H. Wang[2], Y. F. Wang[2], N. Bonini[3†], N. Marzari[3†], N. Pugno[4,5], G. Savini[5], A. Lombardo[5] and A. C. Ferrari[5]*

The quest for materials capable of realizing the next generation of electronic and photonic devices continues to fuel research on the electronic, optical and vibrational properties of graphene. Few-layer graphene (FLG) flakes with less than ten layers each show a distinctive band structure. Thus, there is an increasing interest in the physics and applications of FLGs. Raman spectroscopy is one of the most useful and versatile tools to probe graphene samples. Here, we uncover the interlayer shear mode of FLGs, ranging from bilayer graphene (BLG) to bulk graphite, and suggest that the corresponding Raman peak measures the interlayer coupling. This peak scales from $\sim43\,cm^{-1}$ in bulk graphite to $\sim31\,cm^{-1}$ in BLG. Its low energy makes it sensitive to near-Dirac point quasiparticles. Similar shear modes are expected in all layered materials, providing a direct probe of interlayer interactions.

Single-layer graphene (SLG) has high mobility and optical transparency, as well as flexibility, robustness and environmental stability[1,2]. These intriguing properties extend to multi-layers. Bilayer graphene (BLG) is a tunable band gap semiconductor[3], trilayer graphene (TLG) has a unique electronic structure consisting, in the simplest approximation, of massless SLG and massive BLG subbands[4–6]. Few-layer graphene (FLG) with less than ten layers each show a distinctive band structure[6]. There is thus an increasing interest in the physics of FLGs, with or without Bernal stacking[7–9], and their application in useful devices. For example, as SLG absorbs 2.3% of the incident light[10], FLG can be used to surpass the transmittance of indium tin oxide[2], and to engineer near-market transparent conductors[11], exploiting the lower sheet resistance afforded by combining more than one SLG (refs 2,11). The layers can be stacked as in graphite, or have any orientation. This gives rise to a wealth of electronic properties, such as the appearance of a Dirac spectrum even in FLG (ref. 12).

Raman spectroscopy is one of the most useful and versatile tools to probe graphene samples[13,14]. The measurement of the SLG, BLG and FLG Raman spectra[13] triggered a huge effort to understand phonons, electron–phonon, magneto-phonon and electron–electron interactions, and the influence on the Raman process of number and orientation of layers, electric or magnetic fields, strain, doping, disorder, edges and functional groups[14].

The SLG phonon dispersions comprise three acoustic and three optical branches. A necessary, but not sufficient, condition for a phonon mode to be Raman active is to satisfy the Raman fundamental selection rule, that is, to be at the Brillouin Zone centre, Γ, with wave vector $\mathbf{q} \approx \mathbf{0}$ (ref. 15). SLG has six normal modes at Γ: $A_{2u} + B_{2g} + E_{1u} + E_{2g}$ (ref. 16). There are two degenerate in-plane optical modes, E_{2g}, and one out-of-plane optical mode B_{2g} (ref. 16). E_{2g} modes are Raman active, whereas B_{2g} is neither Raman nor infrared active[16]. In the case of graphite there are four atoms per unit cell, and only half of them have fourth neighbours that either lie directly above or below in adjacent layers. Therefore the two atoms of the unit cell in each layer are now inequivalent. This doubles the number of optical modes, and is responsible for the infrared activity of graphite[16]. All SLG optical modes become Davydov doublets in graphite: E_{2g} generates an infrared-active E_{1u} and a Raman-active E_{2g}, B_{2g} goes into an infrared-active A_{2u}, and an inactive B_{2g}. The zone boundary acoustic modes fold back to the zone centre as rigid layer modes: an optically inactive B_{2g} and a Raman-active E_{2g}. The acoustic modes remain E_{2u} and E_{1u} (ref. 16). Thus for graphite[16,17] $\Gamma = 2(A_{2u} + B_{2g} + E_{1u} + E_{2g})$. There are now two Raman-active E_{2g} modes, each doubly degenerate. The high-frequency E_{2g} mode is responsible for the well known G peak, measured and discussed in thousands of papers so far for any carbon allotrope[18].

Here we focus on the low-energy E_{2g} mode. This is a doubly degenerate rigid layer shear mode, involving the relative motion of atoms in adjacent planes. It was first measured in 1975 by Nemanich et al.[19] in bulk graphite at $\sim42\,cm^{-1}$. We uncover the equivalent mode for FLGs and show that it provides a direct measurement of the interlayer coupling. For this reason we name C the corresponding Raman peak. On one hand, the C peak energy, $E(C) \sim 5\,meV$, is much lower than the notch and edge filter cuts of most Raman spectrometers, and its intensity is much smaller than the G peak. This explains why it was not seen thus far in FLG and, even for graphite, it was reported in only a handful of papers[19–21], with no firm agreement on position and width. On the other hand, this makes it a probe for the quasiparticles near the Dirac point by quantum interference.

The traditional approach to performing very low energy Raman measurements involves the use of a triple spectrometer. However, this greatly reduces the signal intensity compared with the combination of a single monochromator and a notch filter, although the latter arrangement usually does not allow one to detect modes below ~30–$40\,cm^{-1}$. Here we show that detection of Raman modes down to $\sim10\,cm^{-1}$ is possible using three BragGrate notch filters (BNF) in combination with a single monochromator, as shown in the schematic of Fig. 1a. This set-up is simple, relies on commercial components, and enables us to obtain good signals with low excitation power and short acquisition times (see Methods).

The easiest way to get high-quality FLG is by graphite exfoliation[22] on SiO_2/Si, to enhance visibility[23,24]. Often the Si is doped, for use as a back gate[22]. However, this poses a problem for low-frequency Raman measurements. The incident light can excite carriers in doped Si, producing a strong background[25] that can overshadow the signal of FLG with less than six layers. One approach to overcome this issue is to perform polarized Raman

---

[1]State Key Laboratory of Superlattices and Microstructures, Institute of Semiconductors, Chinese Academy of Sciences, Beijing 100083, China, [2]Department of Physics, Nankai University, Tianjin 300071, China, [3]Department of Materials, University of Oxford, Oxford OX1 3PH, UK, [4]Department of Structural Engineering and Geotechnics, Politecnico di Torino, 10129 Torino, Italy, [5]Engineering Department, Cambridge University, Cambridge CB3 0FA, UK. †Present Addresses: Department of Physics, King's College London, Strand, London WC2R 2LS, UK (N.B.); Theory and Simulation of Materials, École Polytechnique Fédérale de Lausanne, 1015 Lausanne, Switzerland (N.M.). *e-mail: phtan@semi.ac.cn; acf26@eng.cam.ac.uk.
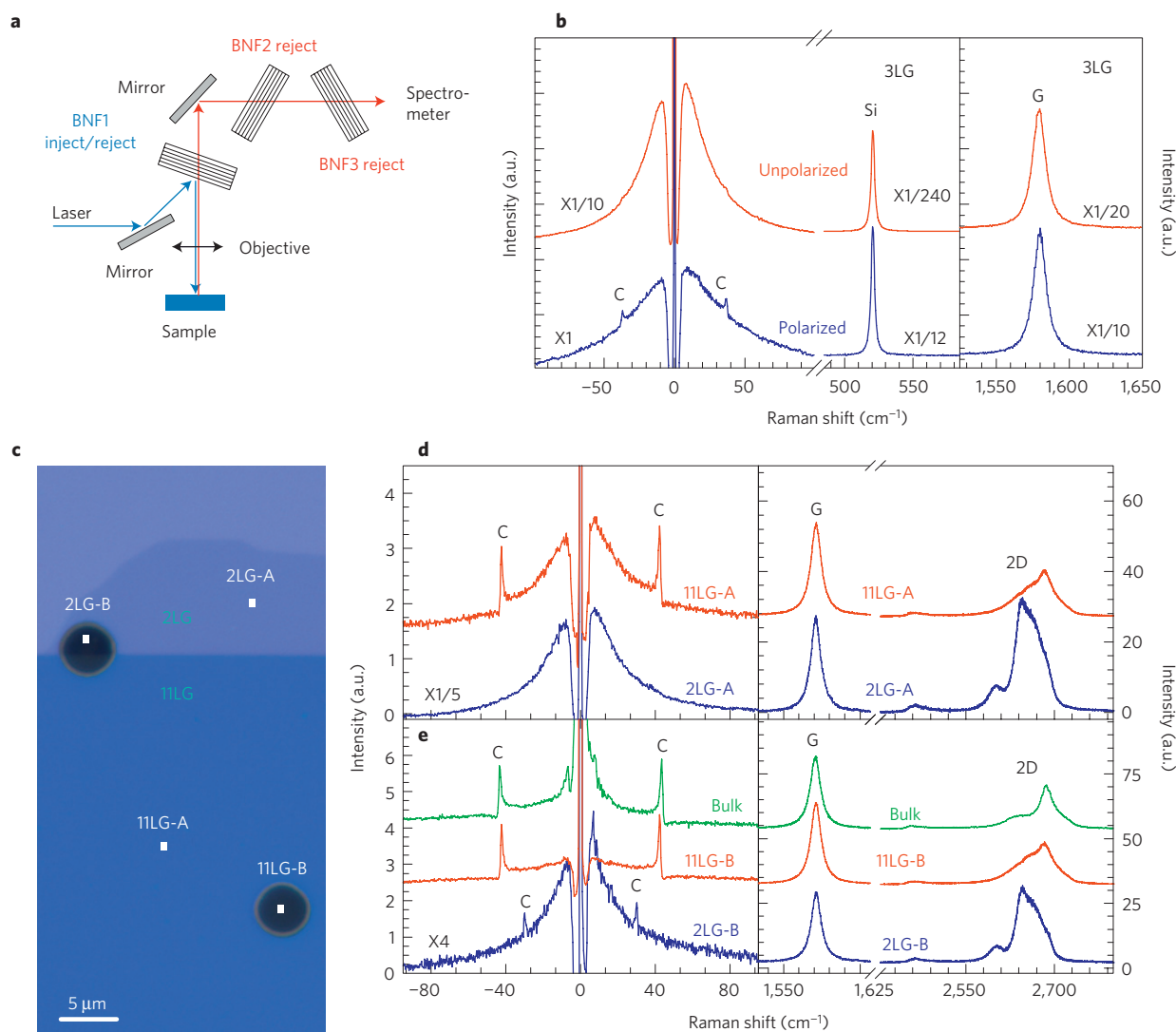
Figure 1 | Raman set-up and spectra of supported and suspended multilayers. a, Schematic diagram of our single monochromator with three BragGrate notch filters (BNF). **b**, Unpolarized and polarized Raman spectra of 3LG on $SiO_2/Si(001)$ in the C peak region (left) and in the G peak region (right). **c**, Optical micrograph of FLG sample. 2LG-A/11LG-A and 2LG-B/11LG-B denote supported and suspended flakes, respectively. **d**, S/AS spectra of supported flakes in the C peak region (left) and S spectra in the G/2D peaks region (right). **e**, S/AS spectra of suspended flakes in the C peak region (left) and S spectra in the G/2D peaks region (right).

measurements, as this background is strongly suppressed in cross polarization[25]. Figure 1b shows the unpolarized (top graph) and polarized (bottom graph) Raman spectra of 3LG on $SiO_2/Si(001)$, with incident light along [1 $\bar{1}$ 0] and scattered light analysed along [1 1 0]. A large substrate background is observed in the unpolarized measurement, whereas in the polarized measurement the Si mode and its low-frequency background are suppressed, thus revealing a peak at $\sim 37\,cm^{-1}$. However, polarized Raman spectra have a lower intensity and a different 2D to G ratio compared with unpolarized ones. Therefore, to collect the highest quality C peak data in unpolarized measurements, we take a different route. We use low-doped Si (resistivity $\geq 2,000\,\Omega\,cm$) and suspend the FLG on ~ 2–$5\,\mu m$ holes, as shown in Fig. 1c. The number of layers and their stacking are identified by a combination of 2D peak Raman spectroscopy[7,13] and optical contrast on the supported section of the flake[23,24]. Figure 1d,e plot the Stokes (S) and anti-Stokes (AS) spectra for supported and suspended BLG, 11LG and bulk graphite. We use the notation NLG to indicate FLG with N layers. Thus 1LG = SLG; 2LG = BLG, 3LG = TLG, and, for example, 11LG means 11 layers. In the suspended flakes the C peak is clearly seen. On the other hand,

the supported ones show the Si background, Fig. 1d (left). Although for 11LG and bulk this does not overshadow the C peak, for fewer layers this covers the C peak to the point that in supported BLG it is difficult to detect the C peak for unpolarized measurements.

We calibrate the C peak position, Pos(C), as follows. We first set the Rayleigh line as $0\,cm^{-1}$. Given the low E(C), the S/AS intensity ratio is close to unity. Similar to the G peak[26,27], but unlike the D and 2D peaks[26,27], the S/AS C peaks are symmetric relative to the Rayleigh line, thus we take $Pos(C) = [Pos(C)_S + Pos(C)_{AS}]/2$. We obtain $Pos(C) \sim 31\,cm^{-1}$ for BLG, $\sim 42.7\,cm^{-1}$ for 11LG and $\sim 43.5\,cm^{-1}$ for bulk graphite. By assuming a Lorentzian lineshape, we derive a full-width at half-maximum, FWHM(C), $\sim 1.2\,cm^{-1}$. Considering the $\sim 0.5\,cm^{-1}$ spectral broadening of our spectrometer, we derive an intrinsic linewidth $\sim 0.7\,cm^{-1}$. From the S/AS ratio[15] we estimate the local T on the sample, $T = \hbar\omega/k_B \ln\{I(C)_S/I(C)_{AS} \cdot \{[\omega_L + Pos(C)]/[\omega_L - Pos(C)]\}^4\}$, where $\hbar$ is the reduced Planck constant, ω_L is the laser frequency, k_B is the Boltzmann constant and $I(C)_S/I(C)_{AS}$ is the C peak S/AS intensity ratio. This gives $T \sim 300\,K$, indicating negligible laser heating.
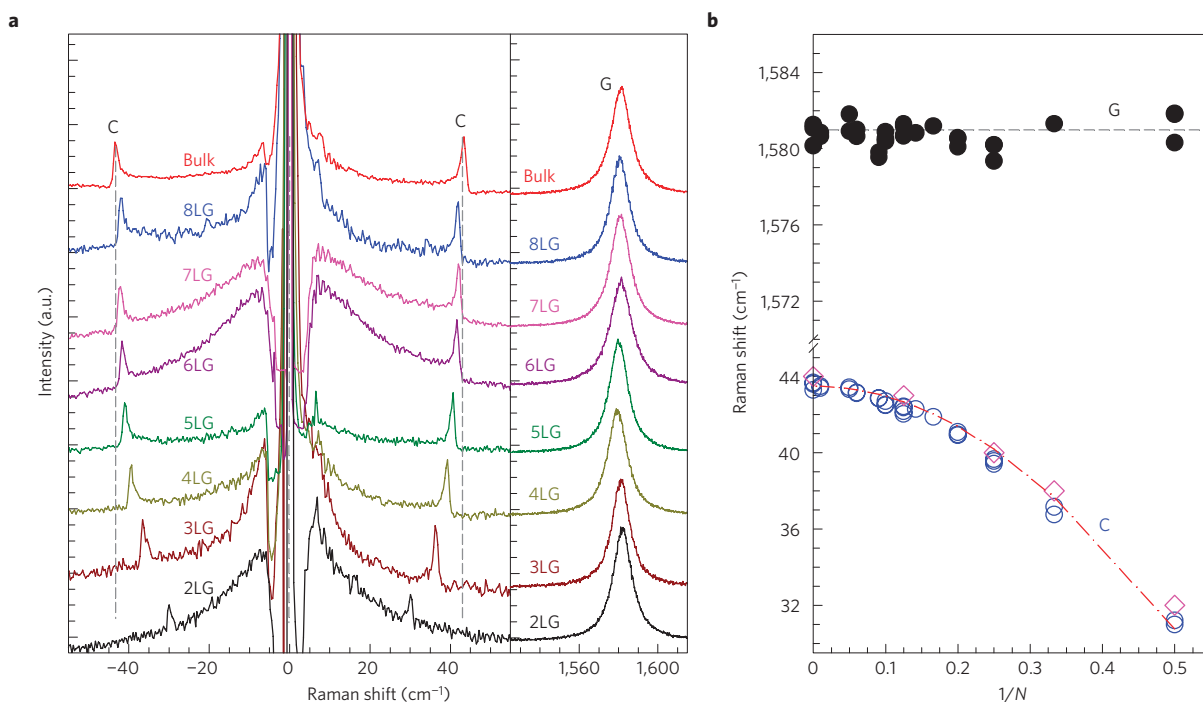
295

Figure 2 | Raman spectra and fits of the C and G peaks as a function of number of layers. a, S/AS Raman spectra for the C peak spectral region (left) and S Raman spectra for the G peak spectral region (right). **b**, Peak positions Pos(G) (filled black circles) and Pos(C) (open blue circles), as a function of inverse layer number. The red dash–dotted line is a plot of equation (2), open diamonds are DFT calculations. Vertical dashed lines in **a** and the horizontal line in **b** are guides to the eye.

Figure 2a plots the Raman spectra for a set of samples of increasing thickness. Figure 2b shows the fitted Pos(G) and Pos(C) as a function of $1/N$, where N is the number of layers. Whereas Pos(G) remains $\sim 1{,}581\,\mathrm{cm}^{-1}$, with no significant change with N, Pos(C) increases from BLG to bulk graphite. Note that in Fig. 2b the spectral range used to plot the G and C peak data is the same ($16\,\mathrm{cm}^{-1}$), thus the C peak shift with N is truly representative of its much stronger variation compared with G. $I(\mathrm{C})/I(\mathrm{G})$ at 633 nm, after calibration to take into account the different response of our system in the C and G peak spectral regions, is approximately 0.0052, 0.044 and 0.049, and the ratio of the integrated peak areas, $A(\mathrm{C})/A(\mathrm{G})$, is approximately 0.00038, 0.0023 and 0.0034, for BLG, 11LG and bulk graphite, respectively. These slightly change with excitation energy, for example, $I(\mathrm{C})/I(\mathrm{G}) \sim 0.025$ and $A(\mathrm{C})/A(\mathrm{G}) \sim 0.00096$ for bulk graphite at 532 nm. Because these ratios depend on the electron phonon coupling (EPC), this immediately indicates that EPC(C) is much smaller than EPC(G).

The Pos(C) dependence on the number of layers can be explained by considering a linear-chain model. For FLG with N layers, there are $2N$ atoms per unit cell. The corresponding in-plane optical modes consist of N degenerate pairs of in-plane stretching modes, and $N-1$ degenerate pairs of in-plane shear modes between neighbouring layers. We assume that a layer interacts strongly only with adjacent layers and that the strength of this interlayer coupling is characterized by an interlayer force constant per unit area, α. The $N-1$ shear modes of an NLG can be computed by diagonalizing the corresponding $N \times N$ (tridiagonal) dynamical matrix. The frequency ω_i (in cm^{-1}) of the ith vibrational mode is given by

$$\omega_i^2 = \frac{1}{2\pi^2 c^2}\frac{\alpha}{\mu}\left\{1-\cos\left[\frac{(i-1)\pi}{N}\right]\right\} \tag{1}$$

where $i = 2, \dots, N$, $\mu = 7.6 \times 10^{-27}\,\mathrm{kg\,\AA^{-2}}$ is the SLG mass per unit area and c is the speed of light in $\mathrm{cm\,s}^{-1}$. The corresponding

ith displacement eigenvector $v_j^{(i)}$ is given by

$$v_j^{(i)} = \cos\left[\frac{(i-1)(2j-1)\pi}{2N}\right]$$

where j labels the layers. The highest frequency mode (for $i=N$) is Raman active. Here adjacent layers move out of phase in the direction parallel to the planes. In the case of graphite, $N \rightarrow \infty$ and $\omega_\infty = \mathrm{Pos(C)}_\infty = (1/\pi c)\sqrt{\alpha/\mu}$. This is the doubly degenerate E_{2g} shear mode responsible for the C peak (Fig. 3a). Thus, $\mathrm{Pos(C)}_N$ (in cm^{-1}) for an NLG is given by equation (1), setting $i=N$:

$$\mathrm{Pos(C)}_N = \frac{1}{\sqrt{2}\pi c}\sqrt{\frac{\alpha}{\mu}}\sqrt{1+\cos\left(\frac{\pi}{N}\right)} \tag{2}$$

In BLG, $N=2$, and $\mathrm{Pos(C)}_2 = (1/\sqrt{2}\pi c)\sqrt{\alpha/\mu}$, that is $\sqrt{2}$ smaller than $\mathrm{Pos(C)}_\infty$, corresponding to bulk graphite, in excellent agreement with the experiments. In fact, the dash–dotted line in Fig. 2b shows that equation (2) describes all the experimental data, thus validating our simple model. The only unknown parameter in equation (2) is the interlayer coupling strength. By fitting the experimental data we can directly measure it. We find $\alpha \sim 12.8 \times 10^{18}\,\mathrm{N\,m}^{-3}$. This implies that, in Bernal-stacked FLG, the hardening of the C mode is not due to a variation of interlayer coupling, but rather to an increase of the overall restoring force (surface layers are less bound than in the bulk) going from BLG to bulk graphite. For a given N, we expect variations of Pos(C) if the interlayer coupling is modified, for example by changing the spacing or relative layer orientation (in the latter case we also expect mode splitting).

These results are further confirmed by *ab initio* calculations performed using density functional theory (DFT) and density functional perturbation theory (DFPT), as discussed in Methods.

Figure 3b plots the in-plane shear modes for 2LG through to 5LG and bulk graphite. For a given N, there are $N-1$ shear modes,
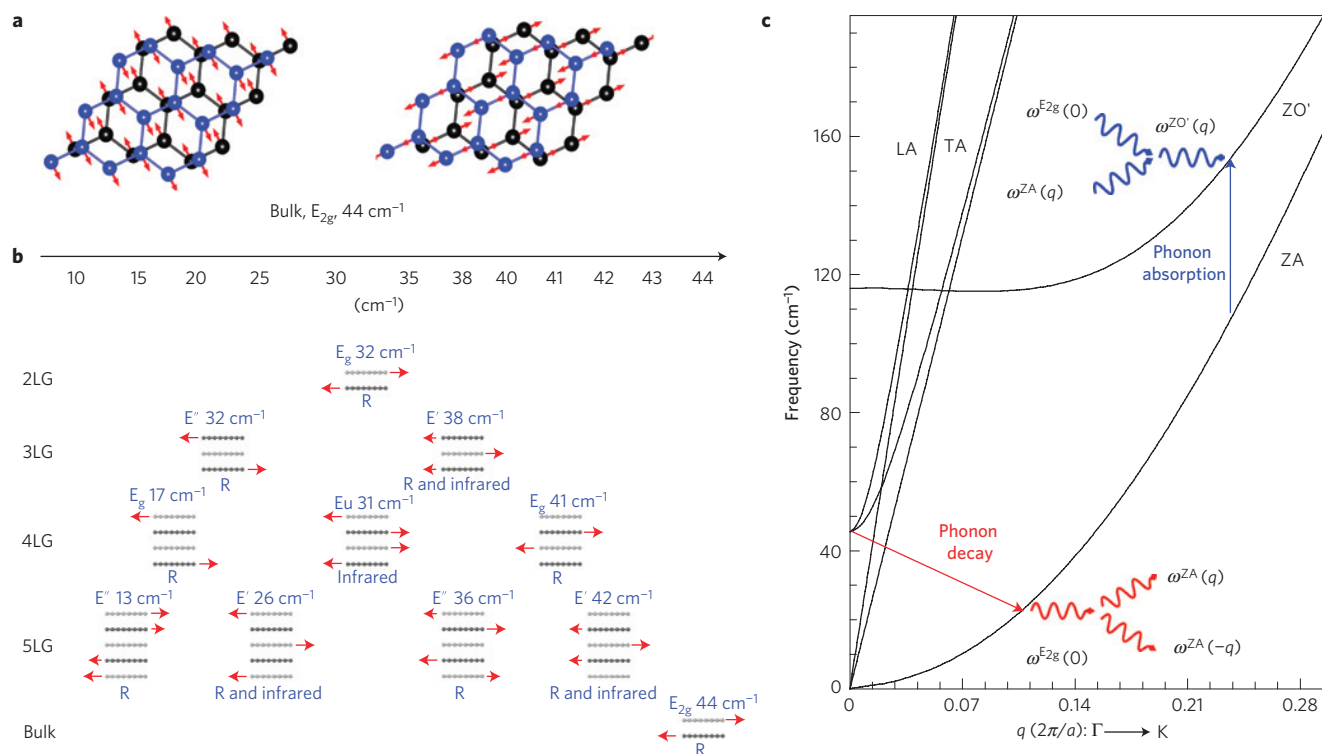
Figure 3 | Normal mode displacements and anharmonic decay channels. a, The two degenerate E_{2g} modes in graphite. **b,** Symmetry, *ab initio* frequencies and normal mode displacement for each shear mode. The Raman-active (R) and infrared-active modes are identified. **c,** Schematic representation of the anharmonic decay channels for the C mode in bulk graphite.

which can be Raman-active, infrared-active or both, but, for $N > 2$, $N − 2$ of those have a different displacement pattern compared to the C mode, as not all the neighbouring layers vibrate out of phase. The highest frequency Raman-active mode corresponds to the C peak. We expect the other Raman-active modes to have a much weaker intensity than the C peak, as a result of a smaller EPC, also confirmed by DFT. More work is needed to detect those modes.

We get an excellent agreement between our DFT frequencies and the experimental data, as indicated by the open diamond symbols in Fig. 2b. This might seem surprising, because local or semi-local exchange correlation functionals may not properly describe van der Waals (VdW) interactions[28], and more sophisticated approaches are necessary to accurately describe the interlayer bonding and equilibrium distance in graphitic materials (see ref. 29 and references therein). However, it was shown that in bulk graphite all phonon dispersions are well-described by DFT, both in local density approximation (LDA) and in the generalized gradient approximation (GGA), even in the absence of VdW interactions in the functional, provided that the correct geometry (that is, interlayer spacing) is used[30]. This occurs because VdW interactions can give a significant contribution to the total energy (hence determining the ratio, Ra, between the interlayer spacing and in-plane lattice constant), but give a negligible contribution to second derivatives (that is, the phonons). Thus, if the correct geometry is used, phonon dispersions are reproduced well. LDA does provide excellent geometries: in graphite $Ra = 2.725$, 2.74 and 2.91, as derived from experiments, LDA and VdW-DFT respectively, whereas for BLG, LDA and VdW-DFT give $Ra = 2.74$ and 2.90. LDA consistently predicts a smaller value than VdW-DFT, but in excellent agreement with experiments. This is confirmed, independently, for bulk graphite and any FLG, by the very good agreement between our LDA calculations and the measured FLG C modes. It is also important to stress that both LDA and VdW-DFT predict the same interlayer spacing for AB-stacked systems. This is consistent with our

interpretation that the hardening of the C mode when going from Bernal-stacked BLG to graphite is not a result of a variation of the interlayer distance and coupling strength with the number of layers.

Our measured α gives further physical insights into FLG. We note that α is a shear force per unit area. Thus, by definition of shear force, $F = \alpha Ax$, where A is the graphene surface area and x is the shear displacement. According to classical definitions in elasticity[31], we also have that the mean shear stress is $\tau = F/A$ and, for small displacements, the mean shear strain is $\gamma = x/t$, where t is the equilibrium distance between two adjacent graphene layers. Also, by definition, the shear modulus of the layer–layer interface is $C_{44} = \tau/\gamma$. Thus, α is linked to the shear modulus as $C_{44} = \alpha t$. From our measurements we get $C_{44} = 4.3$ GPa for graphite, consistent with previous reports giving values between 4.5 and 5.1 GPa (refs 32,33). On the other hand, the C peak allows the shear modulus for FLG of any number of layers to be probed for the first time. This analysis could be extended to any layered material, deducing the corresponding elastic constants still unknown.

As the C peak corresponds to a E_{2g} mode at Γ, it is not expected to be dispersive with excitation energy, unlike the D, D′, D″ peaks and their overtones[14]. This is confirmed in Fig. 4a, where the C peak does not shift for the three excitation wavelengths: 785, 633 and 532 nm.

We now consider FWHM(C). Two factors contribute to the linewidth of the E_{2g} Raman modes in graphene and graphite: the EPC term[34,35] and anharmonic phonon–phonon interactions[36]. In the absence of doping, FWHM(G) $\sim$12–14 cm^{-1} in SLG and bulk graphite, mostly due to the dominant EPC contribution[34,35], the phonon–phonon contribution being $\sim$1.7 cm^{-1} (ref. 36). The experimental FWHM(C) is much smaller, not just in comparison with the overall FWHM(G), but also with respect to the non-EPC component of FWHM(G). This immediately indicates a much smaller EPC(C) than EPC(G), consistent with the much smaller C peak intensity. Our DFT calculations give FWHM(C) ~ 0.3 cm^{-1}
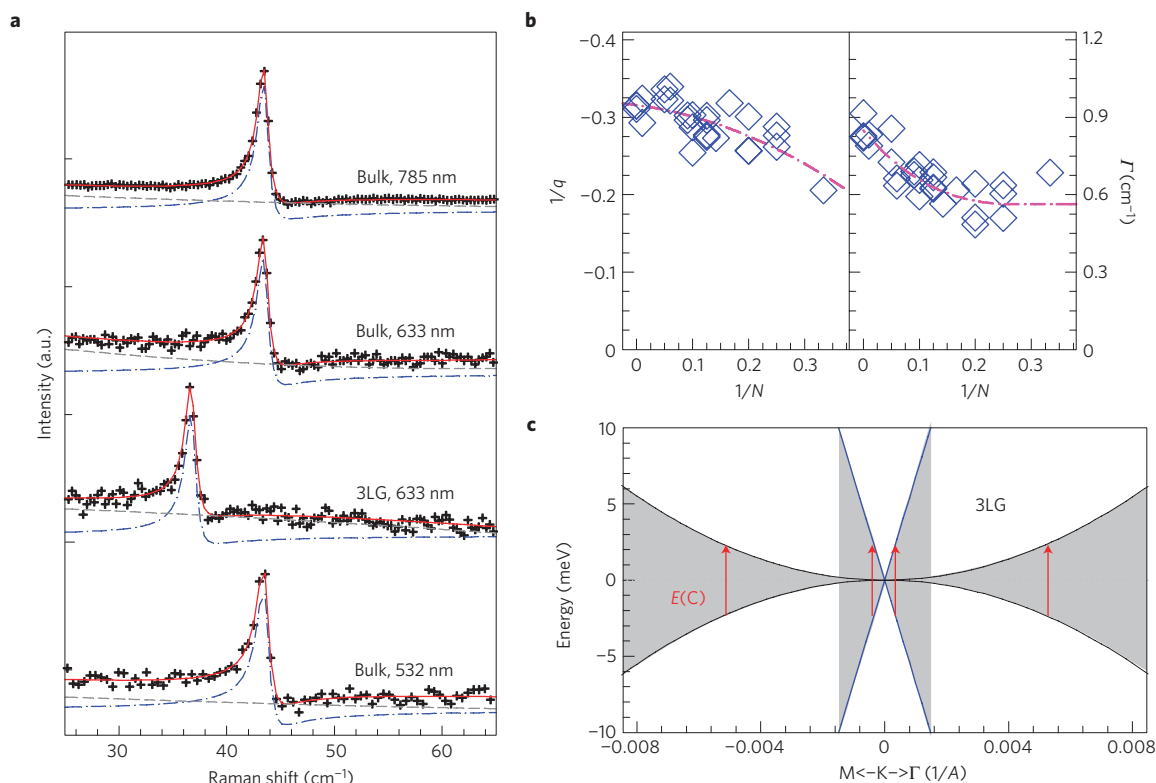
Figure 4 | BWF lineshape of the C peak. a, C peaks with BWF fit for bulk graphite and 3LG. Fitted curve (solid red lines); background (dashed lines); BWF component (dash–dotted lines). **b**, Fitted $1/q$ (left) and Γ (right) as a function of inverse layer number. Note that $0.5\ cm^{-1}$ was subtracted from Γ to account for the system resolution. The dash–dotted lines are guides to the eye. **c**, Schematic band structure of 3LG close to K. The grey regions highlight transitions near K that could resonate with the C mode. Red arrows indicate transitions with the same energy as the C mode, $E(C)$.

at 300 K in graphite, in reasonable agreement with experiments, the EPC contribution being $\sim0.05\ cm^{-1}$ and the phonon–phonon contribution being $\sim0.25\ cm^{-1}$. The anharmonic term consists of three-phonon decay (30% of the total anharmonic linewidth at 300 K) and absorption (70%) processes. The shear mode splits mainly into two out-of-plane ZA bending modes, at $\mathbf{q}$ and $-\mathbf{q}$, close to $\boldsymbol{\Gamma}$. The absorption processes are dominated by the merging of the shear mode and a ZA mode into an out-of-plane ZO′ bending mode (the prime indicates an optical mode where the two atoms in each layer of the unit cell of graphite vibrate together, but out of phase with respect to the two atoms of the other layer) (Fig. 3c). We expect the anharmonic linewidth not to change significantly in NLG, as the available phase space of decay/absorption channels in these systems is very similar to graphite. Also, our calculations for BLG, TLG and 4LG show that the EPC contribution to the linewidth is nearly independent of the number of layers. Thus, DFT indicates that the overall FWHM does not change significantly with N, in agreement with experiments. Note that, if we take a 4LG as an example, the EPC contribution to FWHM(G) is ~150 times larger than for FWHM(C). In turn, this is ~15 times larger than the EPC contribution to the other Raman-active shear mode at $\sim17\ cm^{-1}$, confirming the expectation that the other C modes would be challenging to detect.

We now examine more closely the C peak shape. This can be well-fitted with a Breit–Wagner–Fano (BWF), as shown, for example, in the case of 3LG and bulk graphite in Fig. 4a. In general, this arises as quantum interference between a Raman-allowed phonon and a continuum of Raman-active electronic (or multiphonon) transitions[37]. The BWF lineshape is given by[37]

$$I(\omega) = I_0 \frac{[1+2(\omega-\omega_0)/(q\Gamma)]^2}{[1+4(\omega-\omega_0)^2/\Gamma^2]}$$

where I_0, ω_0, Γ and $1/|q|$ are the intensity, uncoupled mode frequency, broadening parameter and coupling coefficient. The peak maximum is at $\omega_{max} = \omega_0 + \Gamma/2q$ and its FWHM $= \Gamma(q^2+1)/|q^2-1|$. In the limit $1/q \to 0$, a Lorentzian lineshape is recovered, with FWHM $= \Gamma$ and $\omega_{max} = \omega_0$. The fitted $1/q$ and Γ are summarized in Fig. 4b. Pos(C) in the BWF fit is $\Gamma/2|q|$ ($\sim0.3\ cm^{-1}$) higher than in a Lorentzian fit.

We find a smaller $1/|q|$ when we use a laser power high enough to shift the G peak, that is, to heat the sample. Thus, in our low-power experiments, the possible laser-induced electron–hole plasma is not the cause of the observed BWF lineshape. We also find that the C peak of bulk graphite at 77 K has the same q as at room temperature, in contrast to what would be expected if the BWF were due to a multiphonon resonance[38]. We thus attribute the BWF lineshape to quantum interference between the C mode and a continuum of electronic transitions near the K point. The band structure of Bernal-stacked FLGs can be decomposed into groups of BLG bands, with different effective masses, plus—for odd layer numbers—a pair of SLG bands[6]. Figure 4c plots, as an example, a simplified band structure of 3LG in a range of the order of the C phonon energy, $E(C)$, and identifies electronic transitions which can couple with the C mode. Because the density of states with energy higher than $E(C)$ is much larger than that with energy smaller than $E(C)$, q is not expected to change significantly from BLG to bulk graphite, in agreement with our findings. If the Fermi energy, E_F, is larger than $E(C)/2$, the resonance with the C mode would become weaker, eventually leading to the disappearance of the BWF profile. Figure 4b shows that $1/|q|$ and the linewidth decrease slightly with decreasing N. It is known that the top and bottom layers of NLG flakes can be doped by absorption of air molecules or charge transfer from the substrate[35,39,40]. This would reduce the coupling between the C mode and the transitions below $2E_F$. Therefore, the trend

observed in Fig. 4b can be assigned to the higher influence of adsorbates and charge transfer for a lower number of layers.

As discussed above, FWHM(G) is much larger than FWHM(C), owing to the much larger EPC and phonon–phonon contributions. The EPC dominates FWHM(G), and the G peak is always Lorentzian.

In summary, we have revealed the Raman signature of the interlayer shear mode of FLG. Graphite is not the only layered material. Transition metal dichalcogenides, transition metal oxides, and other compounds such as BN, Bi_2Te_3 and Bi_2Se_3 can also be exfoliated to produce a whole range of two-dimensional crystals, which are just beginning to be investigated[41]. Similar shear modes are expected in all these materials, and their detection will provide a direct probe of interlayer interactions.

Methods

Raman spectroscopy. Raman measurements are performed in a backscattering geometry using a Jobin-Yvon HR800 Raman system equipped with a liquid nitrogen cooled charge-coupled detector. The laser excitation wavelengths are 785 nm, 633 nm and 532 nm from a Ti-sapphire laser, a HeNe laser and a diode-pumped solid-state laser, respectively. A typical laser power of 0.5 mW is used to avoid sample heating. The laser plasma lines are removed using a BragGrate bandpass filter from OptiGrate Corp., as these would appear in the same spectral range as the C peak. The Rayleigh line is suppressed using three BragGrate notch filters (OptiGrate Corp.) with an optical density 3 and a spectral bandwidth ∼5–10 cm^{-1}. The configuration of the three BragGrate notch filters in the Jobin-Yvon HR800 spectrometer is shown in Fig. 1a, but a similar arrangement can be implemented for other spectrometers. Argon gas is flowed over the sample to remove the low-frequency Raman modes from the air. We use a ×100 objective with NA = 0.90. A 1,800 lines per mm grating enables us to have each pixel of the charge-coupled detector cover ∼0.35 cm^{-1} at 633 nm. A spectral resolution ∼0.6 cm^{-1} is estimated from the FWHM of the Rayleigh peak at 633 nm.

Computational details. Calculations are performed using DFT and DFPT, as implemented in the Plane-Wave Self-Consistent Field (PWscf) package of the QUANTUM-ESPRESSO distribution, within the local density approximation (LDA), and ultrasoft pseudopotentials generated using the Rappe–Rabe–Kaxiras–Joannopoulos (RRKJ) approach. The cutoffs are 40 Ry for the wave functions and 480 Ry for the charge density. The Brillouin zone is sampled on a 42 × 42 × 16 Monkhorst–Pack mesh for bulk graphite and a 42 × 42 × 1 Monkhorst–Pack mesh for SLG and BLG. NLG are modelled using supercell configurations, with periodic replicas separated by a 10 Å vacuum in the perpendicular direction. The electron–phonon and phonon–phonon matrix elements, as well as the anharmonic contribution to the C mode linewidth, are computed using the approach of ref. 36. The EPC contribution to the linewidth is computed using an interpolation based on maximally-localized Wannier functions as implemented in the Electron–Phonon Wannier (EPW) code[42]. This is a computationally efficient approach allowing very fine sampling of the Brillouin zone (meshes of several million points are needed to get accurate phonon linewidths). The structures of BLG and graphite are also investigated using a more sophisticated functional with van der Waals interactions, VdW-DFT (ref. 43). We note that the EPC is defined as for ref. 34 (for a comparison of the different EPC definitions in literature, see Section III of ref. 44)

References

1. Geim, A. K. & Novoselov, K. S. The rise of graphene. *Nature Mater.* **6,** 183–191 (2007).
2. Bonaccorso, F., Sun, Z., Hasan, T. & Ferrari, A. C. Graphene photonics and optoelectronics. *Nature Photon.* **4,** 611–622 (2010).
3. Castro, E.V. *et al.* Biased bilayer graphene: Semiconductor with a gap tunable by the electric field effect. *Phys. Rev. Lett.* **99,** 216802 (2007).
4. Taychatanapat, T., Watanabe, K., Taniguchi, T. & Jarillo-Herrero, P. Quantum Hall effect and Landau level crossing of Dirac fermions in trilayer graphene. *Nature Phys.* **7,** 621–625 (2011).
5. Guinea, F., Castro Neto, A. H. & Peres, N. M. R. Electronic states and Landau levels in graphene stacks. *Phys. Rev. B* **73,** 245426 (2006).
6. Koshino, M. & Ando, T. Electronic structures and optical absorption of multilayer graphenes. *Solid State Commun.* **149,** 1123–1127 (2009).
7. Lui, C. H. *et al.* Imaging stacking order in few-layer graphene. *Nano Lett.* **11,** 164–169 (2010).
8. Zhu, W., Perebeinos, V., Freitag, M. & Avouris, P. Carrier scattering, mobilities, and electrostatic potential in monolayer, bilayer, and trilayer graphene. *Phys. Rev. B* **80,** 235402 (2009).
9. Ye, J. T. *et al.* Accessing the transport properties of graphene and its multilayers at high carrier density. *Proc. Natl Acad. Sci. USA* **108,** 13002–13006 (2011).
10. Nair, R. R. *et al.* Fine structure constant defines visual transparency of graphene. *Science* **320,** 1308 (2008).
11. Bae, S. *et al.* Roll-to-roll production of 30-inch graphene films for transparent electrodes. *Nature Nanotech.* **5,** 574–578 (2010).
12. Latil, S., Meunier, V. & Henrard, L. Massless fermions in multilayer graphitic systems with misoriented layers: *Ab initio* calculations and experimental fingerprints. *Phys. Rev. B* **76,** 201402(R) (2007).
13. Ferrari, A. C. *et al.* Raman spectrum of graphene and graphene layers. *Phys. Rev. Lett.* **97,** 187401 (2006).
14. Ferrari, A. C. Raman spectroscopy of graphene and graphite: Disorder, electron–phonon coupling, doping and nonadiabatic effects. *Solid State Commun.* **143,** 47–57 (2007).
15. Yu, P. Y. & Cardona, M. *Fundamentals of Semiconductors: Physics and Materials Properties* 3rd edn (Springer, 2003).
16. Nemanich, R. J., G Lucovsky, G. & Solin, S. A. Infrared active optical vibrations of graphite. *Solid State Commun.* **23,** 117–120 (1977).
17. Mani, K. K. & Ramani, R. Lattice dynamics of graphite. *Phys. Status Solidi B* **61,** 659–668 (1974).
18. Ferrari, A. C. & Robertson, J. (eds) Raman spectroscopy in carbons: From nanotubes to diamond. *Phil. Trans. R. Soc. A* **362,** 2267–2565 (2004).
19. Nemanich, R. J., Lucovsky, G. & Solin, S. A. in *Proceedings of the International Conference on Lattice Dynamics* (ed. Balkanski, M.) (Flammarion, 1975).
20. Hanfiand, M., Beister, H. & Syassen, K. Graphite under pressure: Equation of state and first-order Raman modes. *Phys. Rev. B* **39,** 12598–12603 (1989).
21. Sinha, K. & Menéndez, J. First- and second-order resonant Raman scattering in graphite. *Phys. Rev. B* **41,** 10845–10847 (1990).
22. Novoselov, K. S. *et al.* Electric field effect in atomically thin carbon films. *Science* **306,** 666–669 (2004).
23. Blake, P. *et al.* Making graphene visible. *Appl. Phys. Lett.* **91,** 063124 (2007).
24. Casiraghi, C. *et al.* Rayleigh imaging of graphene and graphene layers. *Nano Lett.* **7,** 2711–2717 (2007).
25. Chandrasekhart, M., Cardona, M. & Kane, E. O. Intraband Raman scattering by free carriers in heavily doped n-Si. *Phys. Rev. B* **16,** 3579–3595 (1977).
26. Tan, P. H., Deng, Y. M. & Zhao, Q. Temperature-dependent Raman spectra and anomalous Raman phenomenon of highly oriented pyrolytic graphite. *Phys. Rev. B* **58,** 5435–5439 (1998).
27. Tan, P. H. *et al.* Probing the phonon dispersion relations of graphite from the double-resonance process of Stokes and anti-Stokes Raman scatterings in multiwalled carbon nanotubes. *Phys. Rev. B* **66,** 245410 (2002).
28. Toulouse, J., Colonna, F. & Savin, A. Long-range–short-range separation of the electron–electron interaction in density-functional theory. *Phys. Rev. A* **70,** 062505 (2004).
29. Lebègue, S. *et al.* Cohesive properties and asymptotics of the dispersion interaction in graphite by the random phase approximation. *Phys. Rev. Lett.* **105,** 196401 (2010).
30. Mounet, N. & Marzari, N. First-principles determination of the structural, vibrational and thermodynamic properties of diamond, graphite, and derivatives. *Phys. Rev. B* **71,** 205214 (2005).
31. Carpinteri, A. *Structural Mechanics: A Unified Approach* 200–236, 286–331 (Spon, 1997).
32. Grimsditch, M. Shear elastic modulus of graphite. *J. Phys. C* **16,** L143 (1983).
33. Bosak, A. & Krisch, M. Elasticity of single-crystalline graphite: Inelastic X-ray scattering study. *Phys. Rev. B* **75,** 153408 (2007).
34. Lazzeri, M., Piscanec, S., Mauri, F., Ferrari, A. C. & Robertson, J. Phonon linewidths and electron–phonon coupling in graphite and nanotubes. *Phys. Rev. B* **73,** 155426 (2006).
35. Pisana, S. *et al.* Breakdown of the adiabatic Born–Oppenheimer approximation in graphene. *Nature Mater.* **6,** 198–201 (2007).
36. Bonini, N., Lazzeri, M., Marzari, N. & Mauri, F. Phonon anharmonicities in graphite and graphene. *Phys. Rev. Lett.* **99,** 176802 (2007).
37. Klein, M. V. in *Light Scattering in Solids, Topics in Applied Physics* 2nd edn Vol. 8 (ed. Cardona, M.) (Springer, 1975).
38. Dresselhaus, M. S. & Dresselhaus, G. in *Light Scattering in Solids III* (eds Cardona, M. & Güntherodt, G.) (Springer, 1982).
39. Casiraghi, C. *et al.* Raman fingerprint of charged impurities in graphene. *Appl. Phys. Lett.* **91,** 233108 (2007).
40. Zhao, W. J., Tan, P. H., Liu, J. & Ferrari, A. C. Intercalation of few-layer graphite flakes with FeCl$_3$: Raman determination of Fermi level, layer by layer decoupling, and stability. *J. Am. Chem. Soc.* **133,** 5941–5946 (2011).
41. Coleman, J. N. *et al.* Two-dimensional nanosheets produced by liquid exfoliation of layered materials. *Science* **331,** 568–571 (2011).
42. Noffsinger, J. *et al.* EPW: A program for calculating the electron–photon coupling using maximally localized Wannier functions. *Comput. Phys. Commun.* **181,** 2140–2148 (2010).

43. Thonhauser, T. *et al.* Van der Waals density functional: Self-consistent potential and the nature of the van der Waals bond. *Phys. Rev. B* **76,** 125112 (2007).
44. Basko, D. M., Piscanec, S. & Ferrari, A. C. Electron–electron interactions and doping dependence of the two-phonon Raman intensity in graphene. *Phys. Rev. B* **80,** 165413 (2009).

Author contributions

A.C.F. and P.H.T. conceived the project. P.H.T. designed the measurement set-up. P.H.T., W.P.H., W.J.Z and A.L. prepared the samples and performed spectroscopic measurements and analysis. N.B., N.M., G.S., Z.H.W., H.W., K.C., Y.F.W., N.P., P.H.T. and A.C.F. performed *ab initio* calculations and analytic modelling. A.C.F., P.H.T., N.B. and N.M. wrote the paper.

Additional information

The authors declare no competing financial interests. Reprints and permissions information is available online at www.nature.com/reprints. Correspondence and requests for materials should be addressed to P.H.T. or A.C.F.